Three-dimensional global hybrid simulation of dayside dynamics associated with the quasi-parallel bow shock

Y. Lin and X. Y. Wang

Physics Department, Auburn University, Auburn, Alabama, USA

Received 24 May 2005; revised 5 August 2005; accepted 30 September 2005; published 16 December 2005.

[1] A three-dimensional global-scale hybrid simulation is carried out, for the first time, for dynamics of the dayside bow shock-magnetosphere system associated with the quasi-parallel bow shock. A case with IMF along the Sun-Earth line is examined in detail. First, the foreshock waves and the associated shock reformation process are investigated. In particular, the generation and structure of diamagnetic cavities, with a decrease in the magnetic field and density, in the foreshock of the quasi-parallel shock are discussed. Second, the interaction of the foreshock-originated pressure pulses with the dayside magnetosphere is simulated. The diamagnetic cavities that are generated in the turbulent foreshock due to the ion beam plasma interaction are found to lead to strong surface perturbations at the magnetopause. Third, the coupling between the pressure pulses and the magnetosphere is studied. The compressional waves are found to mode convert to shear Alfvén waves and kinetic Alfvén waves through the Alfvén resonance process in nonuniform plasmas. The shear Alfvén waves lead to field line resonance, which corresponds to the fundamental odd resonance wave number, and produce field-aligned currents in the dipole magnetospheric field.

Citation: Lin, Y., and X. Wang (2005), Three-dimensional global hybrid simulation of dayside dynamics associated with the quasi-parallel bow shock, *J. Geophys. Res.*, *110*, A12216, doi:10.1029/2005JA011243.

1. Introduction

[2] The Earth's bow shock is created by the supersonic solar wind flowing onto the geomagnetic field. The front of this shock is curved, standing around the Earth from the dayside. The bow shock is of great interest in space plasma investigation as it contains important physics ranging from kinetic to global scales. Moreover, electromagnetic waves, often turbulent, emitted by the shock are strongly coupled to the global plasma environment of the magnetosphere. The bow shock thus plays an important role in the interaction between the solar wind and the Earth's magnetosphere.

[3] Under a given interplanetary magnetic field (IMF) condition, the curved shock front usually contains both the quasi-parallel shock, where the angle between the IMF and the shock normal is less than 45°, and the quasi-perpendicular shock. Since the shock normal angle is small at the quasi-parallel shock, the downstream thermal ions, as well as the ions reflected at the shock front, can easily backstream along the field lines and penetrate into the upstream region, leading to electromagnetic instabilities associated with ion beams, ion heating, and energetic ions at quasi-parallel shocks [*Hoppe et al.*, 1981; *Tanaka et al.*, 1983; *Sckopke et al.*, 1983; *Gosling and Robson*, 1985; *Fuselier et al.*, 1995]. Pressure pulses are also frequently generated due to the shock intrinsic processes [*Fairfield et al.*, 1990; *Sibeck et al.*, 2001]. These foreshock pressure pulses and waves are carried by the solar wind to the Earth's dayside magnetopause and cause surface waves at the magnetopause and field-aligned currents and ULF pulsations [*Russell et al.*, 1983; *Engebretson et al.*, 1991; *Sibeck et al.*, 2003] in the magnetosphere.

[4] Hybrid simulations, in which ions are treated as fully kinetic particles, have proven to be a powerful and useful tool for the investigation of the nonlinear structure and ion heating of collisionless shocks [e.g., *Thomas et al.*, 1990; *Winske et al.*, 1990; *Scholer and Terasawa*, 1990; *Scholer*, 1993; *Dubouloz and Scholer*, 1995; *Krauss-Varban*, 1995]. These simulations for a planar shock front have found that the structure of quasi-parallel shocks evolves dynamically due to the wave-particle interaction, consistent with observations at the bow shock [*Hoppe et al.*, 1981; *Schwartz et al.*, 1992]. The shocks are found to go through a reformation process constantly and generate low-frequency large-amplitude electromagnetic waves in the upstream and downstream regions due to reflected/backstreaming ions. These waves play an important role in the ion heating of the shock. The steepening of upstream waves and their crashing into the shock are also believed to lead to the short large-amplitude magnetic structures (SLAMS) [e.g., *Schwartz and Burgess*, 1991].

[5] Moreover, our two-dimensional (2-D) global-scale hybrid simulation for the curved bow shock-magnetosphere

0148-0227/05/2005JA011243

system [*Lin*, 2003] shows that diamagnetic cavities, with a low-density and low-magnetic field center bounded by a boundary of high density and high magnetic field, are present in the foreshock region of the quasi-parallel shocks, where ion beams interact with the incoming solar wind plasma. The cavities can also develop into elongated spatial structures along the field lines, with alternate increases and decreases in the density and corresponding in-phase variations in the magnetic field strength. The frequent presence of diamagnetic cavities in front of quasi-parallel shocks has also been observed by satellites [*Wibberenz et al.*, 1985; *Sibeck et al.*, 1989, 2001; *Fairfield et al.*, 1990]. It is found that the magnetic field strength and plasma density are depressed in the cavity by pressures associated with the energetic ions.

[6] Both the observation [*Sibeck et al.*, 2002] and simulation [*Lin*, 2003] indicate that the structure of individual foreshock cavities resembles the diamagnetic cavity obtained in a hybrid simulation by *Thomas and Brecht* [1988], which attributes the cavities to the diamagnetic effects of ions Fermi accelerated within the foreshock. The simulation by *Thomas and Brecht* [1988] shows that when a finite-sized, about a few tens of the ion inertial lengths, and super-Alfvénic plasma beam moves through a background plasma, the waves excited by an electromagnetic ion beam instability can produce an energized plasma, which pushes out the magnetic field and creates a diamagnetic cavity with depressed (enhanced) plasma density and magnetic field at the center (on the edges). Nevertheless, in the global-scale simulation by *Lin* [2003], in which the ion beam exists in a broad region (width $\sim$30 R_E) of the entire foreshock region of the quasi-parallel shock, multiple cavities are formed, with sizes of 1–3 R_E. Moreover, these craters evolve to alternate field-aligned filaments/cavities, with a certain wave number $k_\perp$ perpendicular to the magnetic field.

[7] Although 2-D hybrid simulations for the curved bow shock can depict important multidimensional physics of the shock, the global structure of the bow shock and the coupling of its waves with the magnetospheric system are of 3-D nature. The interaction between the foreshock waves and the magnetosphere could not be studied in our previous 2-D simulation. The purpose of this paper is to investigate the global physics associated with the quasi-parallel shock using a newly developed 3-D hybrid model.

[8] In this paper we first investigate the 3-D structure of the bow shock by using the 3-D global-scale hybrid simulation. The focus is on the dynamic processes associated with the quasi-parallel shock. Then, the interaction of the bow shock-originated pressure pulses with the magnetosphere is studied. The generation of shear Alfvén waves and kinetic Alfvén waves (KAWs) in this interaction is discussed. The outline of the paper is as the following. The simulation model is described in section 2. The simulation results of the bow shock and its coupling to the magnetosphere are presented in section 3. The summary is given in section 4.

2. Simulation Model

[9] The description of the hybrid code can be found in the work of *Swift* [1996]. The 3-D global-scale code used in this study was developed by extending the 2-D version of the code for the dayside bow shock-magnetosheath-magnetosphere system [e.g., *Swift*, 1996; *Lin*, 2003] to 3-D. A spherical coordinate system is used in the simulation. The simulation domain contains the hemispherical plasma regions with GSM $x > 0$, within geocentric distances 4 $R_E \leq r \leq 22$ R_E, while the Earth is located at the origin. A semicone of 20° polar angle around the positive and negative polar axes, which are chosen along the GSM $\pm y$ axes in the calculation, is cut out from the domain to avoid the singular coordinate line along the polar axes. The reason for rotating the polar axis to the y axis is to retain the important regions of dayside cusps in the domain while cutting out the volumes of the 20° semicones, which are now located near the equator. Nevertheless, for the presentation in the following, we use the convention of polar angle θ with respect to the z axis and azimuthal (longitudinal) angle ϕ in the xy projection plane, with $\theta = 0°$ (180°) being the $+z$ ($-z$) axis and $\phi = 0°$ (180°) being the $x = 0$ and $y > 0$ ($y < 0$) plane.

[10] In the hybrid code the ions (protons) are treated as discrete particles, and the electrons are treated as a massless fluid. Quasi charge neutrality is assumed in the simulation. The equation for ion particle motion in the simulation units is given as

$$\frac{d\mathbf{v}_p}{dt} = \mathbf{E} + \mathbf{v}_p \times \mathbf{B} - \nu(\mathbf{V}_p - \mathbf{V}_e), \tag{1}$$

where $\mathbf{v}_p$ is the ion particle velocity, $\mathbf{E}$ is the electric field in units of ion acceleration, $\mathbf{B}$ is the magnetic field in units of the ion gyrofrequency, ν is the collision frequency which is applied to the magnetopause for possible magnetic reconnection, and $\mathbf{V}_e$ and $\mathbf{V}_p$ are the bulk flow velocities of electrons and ion particles, respectively. For the case shown in this paper, the reconnection occurs only at high latitudes. A small current-dependent collision frequency is imposed only for the magnetopause regions in $x < 6$ R_E. For the magnetopause regions of interest, which are subject to the strong impacts of the foreshock pressure pulses, the resistivity $\nu = 0$.

[11] In addition to the particle ions, a cold, incompressible ion fluid is assumed in the magnetosphere and dominant in the inner magnetosphere [*Swift*, 1996]. The number density of the cold ion fluid is assumed to be

$$N_f = (10^5/r^6)N_0, \tag{2}$$

where N_0 is the ion number density in the solar wind. For $r \geq 10$ R_E, the fluid density is set to be zero exactly. Note that in the present model, the inner boundary of the domain is chosen at $r = 4$ R_E as it is rather difficult numerically to handle the small grid sizes near the semiconic boundaries for smaller radius r, and the realistic plasmasphere density profile is not applied. It would be interesting to compare the resulting Alfvén waves and field line resonance that are obtained from our present model with results from more realistic models.

[12] The electric field can be obtained from the electron momentum equation

$$\mathbf{E} = -\mathbf{V}_e \times \mathbf{B} - (1/N)\nabla p_e - \nu(\mathbf{V}_e - \mathbf{V}_i), \tag{3}$$

where $N = N_p + N_f$ is the total ion number density, N_p is the number density of discrete ions, and $\mathbf{V}_i = (N_p/N)\mathbf{V}_p + (N_f/N)\mathbf{V}_f$ is the total ion bulk flow velocity. The electron fluid is assumed to be isothermal, with

$$T_e = const \tag{4}$$

everywhere for simplicity, and thus $\nabla p_e = T_e \nabla N$. Cases have been performed for electron temperature $T_e = 0$ or finite electron beta $\beta_e = 0.5-2.0$ in the solar wind, while the solar wind ion beta $\beta_p = 0.5$. The resulting structures of the bow shock and magnetosheath remain unchanged, except that the parallel electric field in kinetic Alfvén waves cannot exist in the case with $T_e = 0$. In this paper we show a case with a finite T_e corresponding to $\beta_e = 1.0$ in the solar wind. The electron flow speed is evaluated from Ampere's law,

$$\mathbf{V}_e = \mathbf{V}_i - \frac{\nabla \times \mathbf{B}}{\alpha N}, \tag{5}$$

where the charge coupling constant $\alpha = (4\pi e^2/m_i c^2)$, e is the electron charge, and m_i is the ion mass. The magnetic field is advanced in time from Faraday's law

$$\frac{\partial \mathbf{B}}{\partial t} = -\nabla \times \mathbf{E}. \tag{6}$$

[13] The ion gyrofrequency Ω_0 in the solar wind is chosen to be 1.0 s^{-1}, corresponding to an IMF of ~10 nT, where $\Omega_0 = eB_0/m_i$, and B_0 is the magnitude of the IMF. The ion number density is chosen as $N_0 = 12{,}000\ R_E^{-3}$ in the solar wind. The solar wind ion inertial length $\lambda_0 = c/\omega_{pi0}$ is chosen to be 0.1 R_E. Our previous 2-D simulation indicates that the resulting structures of the bow shock are similar for $\lambda_0 = 0.04\ R_E$ and 0.1 R_E. Note that the Alfvén speed in the solar wind is $V_{A0} = \lambda_0 \Omega_0$.

[14] A total of $\sim 3 \times 10^8$ particles are used in a run. The grids are uniformly distributed in the north-south and east-west coordinate directions, with a total of 104 and 130 grid points, respectively. Nonuniform grid spacing Δr is used in the radial direction, with a higher spatial resolution from $r = 8\ R_E$ to 13 R_E, including the regions of the magnetopause boundary layer, magnetosheath, and the bow shock. The grid size $\Delta r \simeq \lambda_0$ in these regions, and $\simeq 1.3\lambda_0$ for $r > 13\ R_E$. About 150–400 particles are used in each cell in the solar wind and the magnetosheath.

[15] We assume that initially the uniform solar wind and IMF occupy the region of $r > 10\ R_E$, and a 3-D dipole field plus an image dipole occupies the geomagnetic region within $r < 10\ R_E$. A transition layer (with a half-width of 1 R_E) exists between the dipole field and the IMF, centered at $r = 10\ R_E$. For this method of the initial setup, a correction of the initial $\mathbf{B}$ field is usually required to guarantee that $\nabla \cdot \mathbf{B} = 0$ is satisfied. The initial temperature of the solar wind ions is assumed to be uniform and isotropic. For the ion particles located in $r < 10\ R_E$, the temperature is assumed to be several tens times the solar wind ion temperature.

[16] A massively parallel computation is performed for this study. In the simulation, the solar wind flows along the $-x$ direction from the frontside boundary at $r = 22\ R_E$. The bow shock, magnetosheath, and magnetopause form from the interaction between the superfast solar wind and the geomagnetic field. Outflow boundary conditions are used at the backside planar boundaries, corresponding to $x = 0$, and the two semiconic boundaries. A perfect conducting boundary is imposed at the inner boundary at $r = 4\ R_E$.

[17] Physical quantities are normalized as follows. The magnetic field B is normalized to the IMF B_0, the ion number densities are normalized to the solar wind density N_0, the flow velocities are normalized to V_{A0}, and the time t is normalized to Ω_0^{-1}. The spatial coordinates are expressed in units of R_E, and the electric field is expressed in units of $V_{A0}B_0$. The thermal pressure is expressed in units of the magnetic pressure $P_{00} \equiv B_0^2/\alpha$, and the temperature is in units of $T_{00} \equiv P_{00}/N_0$.

[18] In this paper we show a case with the IMF cone angle equal to 0°, which results in the existence of quasi-parallel shocks in a large portion of the dayside domain. The results of the bow shock and its coupling to the magnetosphere are analyzed the detail. Other cases with oblique IMF cone angles and various Mach numbers M_A will be presented in a separate paper.

3. Simulation Results of the Quasi-Parallel Bow Shock and Its Coupling to the Magnetosphere

[19] In the case shown, the IMF is along the Sun-Earth line, with $B_{x0} = B_0$ and $B_{y0} = B_{z0} = 0$. The solar wind ion plasma beta is chosen as $\beta_0 = 0.5$. The solar wind flow speed is assumed to be $V_0 = 5V_{A0}$, corresponding to a Mach number $M_A = 5$. A case with the same parameters has also been shown in our 2-D simulation [*Lin*, 2003], and the present 3-D results will be compared with the previous 2-D case.

3.1. Bow Shock and Foreshock Waves

[20] Figure 1 shows the simulation results at $t = 46$. Shown in the left column of Figure 1 are the magnetic field lines in the 3-D domain and the magnetic field contour in the equatorial plane. The right column shows the contours of the ion particle number density N_p in the noon-midnight meridian plane and the equatorial plane (with half of the view blocked) simultaneously. In this case, the average standoff distance of the bow shock, which is ~11.5–13 R_E, is reached at $t \simeq 20$, while the overall shape of the curved shock front is saturated at $t \simeq 30$. The shock front can be identified from the enhanced ion density and magnetic field strength and the deflection of the IMF, which is originally along the x direction. The magnetosheath, which is the downstream region of the bow shock, is surrounding the magnetosphere. The magnetopause is located around $r = 10\ R_E$ along the Sun-Earth line, where the density N_p suddenly decreases and the B field greatly increases. Note that a reconnection between the magnetosheath and magnetospheric field lines on the dayside takes place in the high-latitude region of the northern hemisphere, as can be seen in the field line plot in Figure 1.

[21] In the foreshock region of the quasi-parallel and parallel shocks ($|y| < 15\ R_E$ and $|z| < 15\ R_E$), the back-streaming and reflected ion beams (with beam density ~2–15% of the solar wind density) interact with the denser and colder incoming solar wind plasma, leading to large-amplitude whistler-type electromagnetic waves with wave vector $\mathbf{k}$ nearly parallel to $\mathbf{B}$ in the solar wind frame of reference.

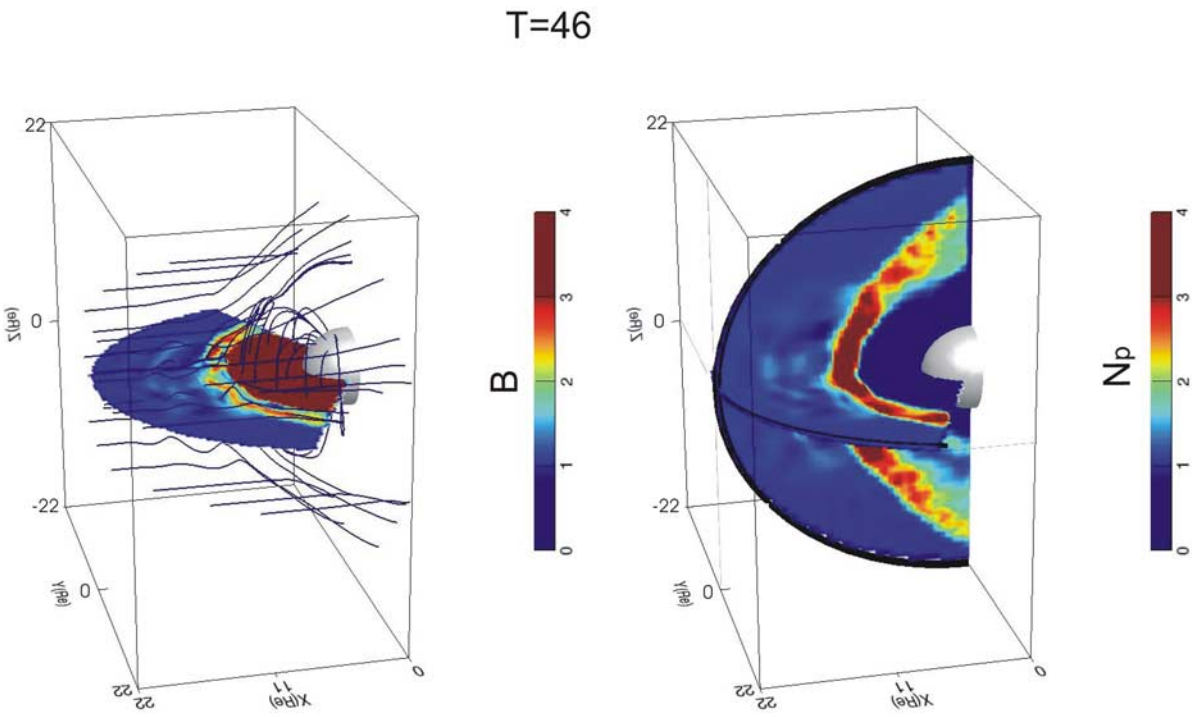

Figure 1. Simulation results at $t = 46$. (left) Some magnetic field lines obtained in the three-dimensional (3-D) domain associated with the quasi-parallel shock, plotted on top of the B field contour in the equatorial plane, and (right) contours of the ion number density N_p in the noon-midnight meridian plane and the equatorial plane.

The field lines are seen waggling in these foreshock waves. The shock front, meanwhile, is going through a constant reformation, or steepening, process due to the transient waves, as shown in previous simulations. In addition, similar to the 2-D simulation by *Lin* [2003], diamagnetic cavities are shown in the foreshock region upstream of the quasi-parallel shocks, as seen in Figure 1. Some of the foreshock cavities are marked in the following Figure 2. The cavity contains a decreased density and decreased magnetic field (by 15–40%) and is often surrounded by enhanced density and magnetic field strength relative to their average values in the solar wind. The spatial variations in B and N_p are in phase and well correlated in these cavities and their surroundings. The ion temperature, on the other hand, is enhanced inside the cavity, while the flow speed decreases. The diamagnetic cavities are essentially a pressure balance structure. Note that in the equator the backside boundaries are along a 20° radial line with respect to the $\pm x$ axis due to the conic simulation boundary.

[22] In order to track the propagation of the foreshock waves to the magnetopause, Figure 2 shows the contour plots of the ion density N_p (left column) and field strength B (right column) obtained at $t = 100$, 105, 110, and 115. The contours are shown for a quarter of the noon-midnight meridian plane (vertical plane, for $x > 0$ and $z > 0$) and equatorial plane (horizontal plane, for $x > 0$ and $y > 0$). Some of the cavities are marked by "a," "b," "c," and "d," as seen for $t = 100$. These foreshock cavities convect to the downstream magnetosheath. At $t = 105$, the cavity "a" has propagated into the magnetosheath. The convection of cavities "b," "c," and "d" are also tracked with time in Figure 2. As the cavity (rim) approaches the magnetopause and is slowed down, it behaves as a dynamic pressure pulse that leads to the expansion (compression) of the magnetopause. The distortion of the magnetopause is seen in the equator around $y \sim 9\ R_E$. The size of the distortion due to the compressional wave pulse is about 3–6 R_E in the east-west and north-south directions. Such local pulse corresponds to a broadband wave spectrum. The arrival of the compressional waves, since much earlier times, causes the compressional and transverse waves in the magnetosphere, as to be discussed in the later subsections. The foreshock diamagnetic cavities are seen to cause maximum surface perturbations among all the arrival compressional structures. The magnetopause surface perturbations mainly propagate in the east-west direction. At $t = 110$, the previous surface perturbation at the magnetopause has propagated to $y \sim 10\ R_E$. At $t = 115$, it has gained a larger tailward

Figure 2. Contours of the ion density N_p (left column) and field strength B (right column), in a quarter of the noon-midnight meridian (vertical) plane and equatorial (horizontal) plane, obtained at $t = 100$, 105, 110, and 115. Some of the foreshock cavities are marked by labels "a," "b," "c," and "d."

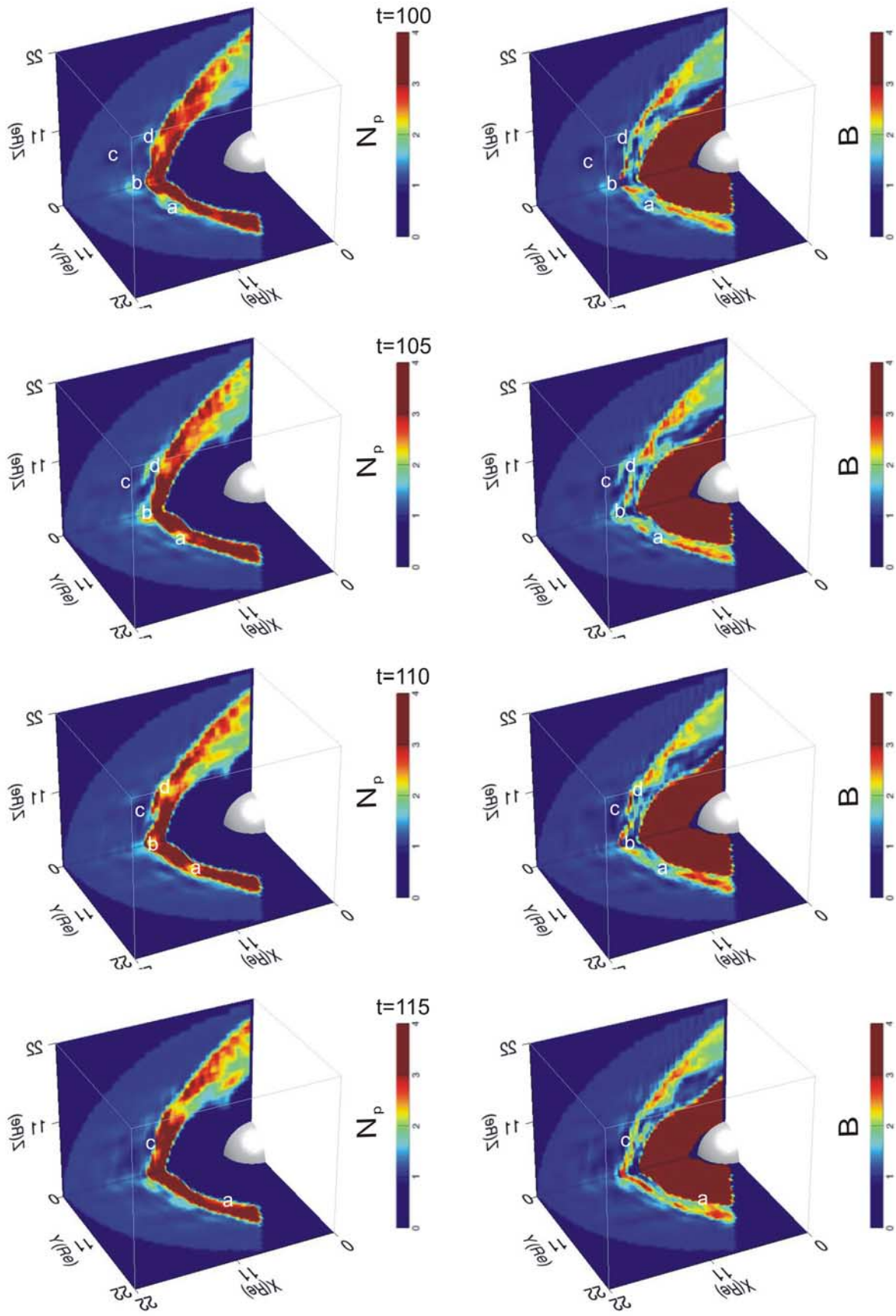

Figure 2

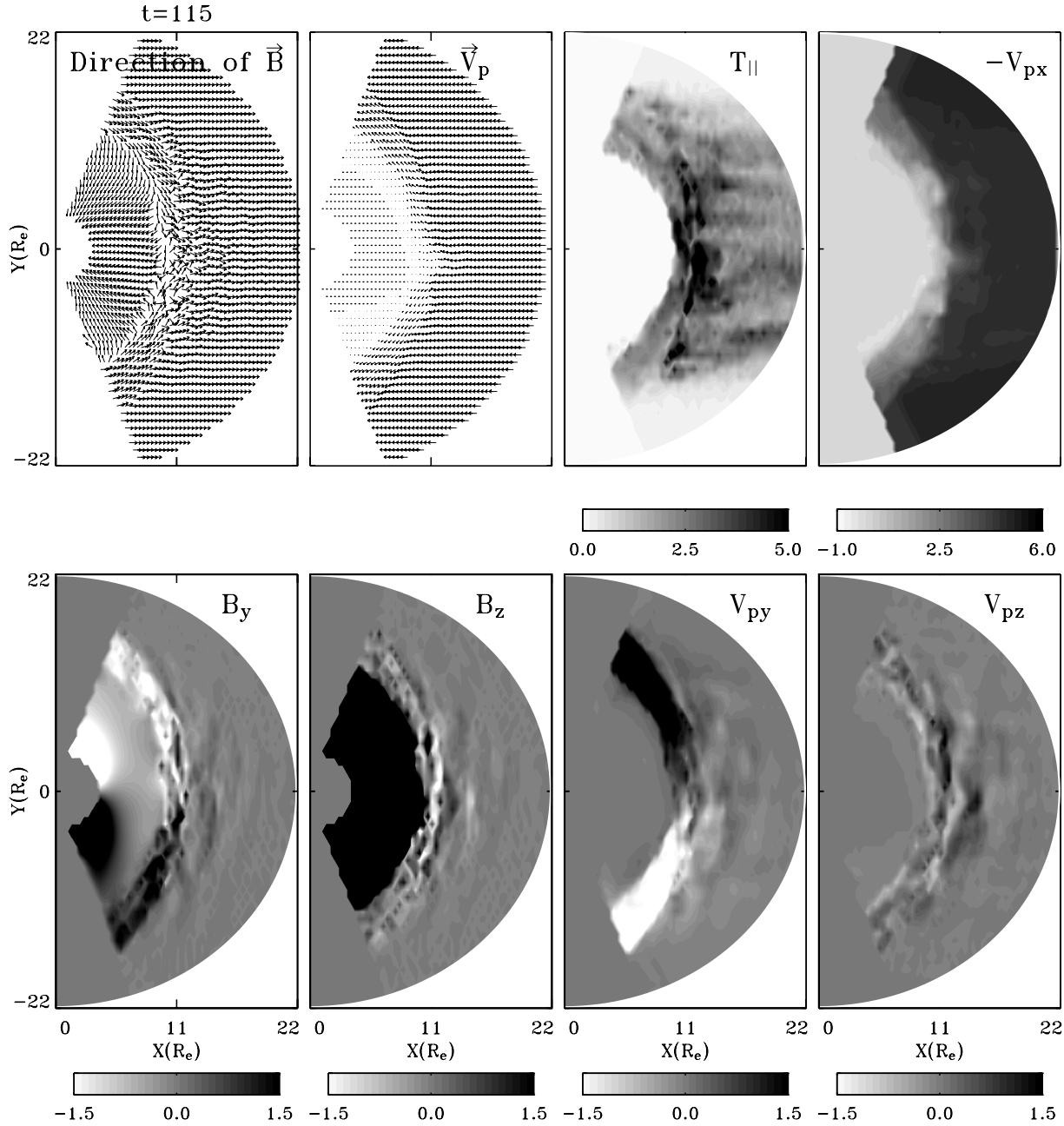

Figure 3. Magnetic field direction, ion flow vectors $\mathbf{V}_p$, and contours of the parallel ion temperature $T_{p\|}$, ion flow component V_{px}, field components B_y and B_z, and flow components V_{py} and V_{pz} in the equatorial plane obtained at $t = 115$.

speed and moved toward the domain boundary. By this time, a second surface distortion also appears at the magnetopause ($y \sim 9\ R_E$) due to a newly arrived cavity structure.

[23] Meanwhile, the foreshock cavities and rims also evolve to structures elongated along field lines, with alternate field-aligned filaments (enhanced density) and cavity-like areas (decreased density) across the field lines, again positively correlated with the B field. Such structures are more obvious in later times, as seen at $t = 115$ in Figure 2. These 3-D but elongated structures, with wave vector $\mathbf{k} \perp \mathbf{B}$, have a width of 1–4 R_E for regions with increased or decreased N_p (or perpendicular wavelength $\lambda \sim 20$–$80c/\omega_{pi}$) in both y and z directions. The presence of the field-aligned structures is also found in the 2-D simulations by *Lin* [2003], although they are 3-D structures as shown in the present simulation. Note that if 1-D passes are made through these 3-D structures, the widths of the regions with density increase or decrease will appear different for different locations of passages. Moreover, different from the 2-D results, these structures, while becoming quasi-stationary in the long run, coexist with the transient cavities even in later times ($t > 150$). The field-aligned structures develop in the foreshock and also extend into the magnetosheath.

[24] The structure of other quantities are shown in Figure 3 for the equatorial plane at $t = 115$. Plotted here are the direction of magnetic field, ion flow vectors $\mathbf{V}_p$, and

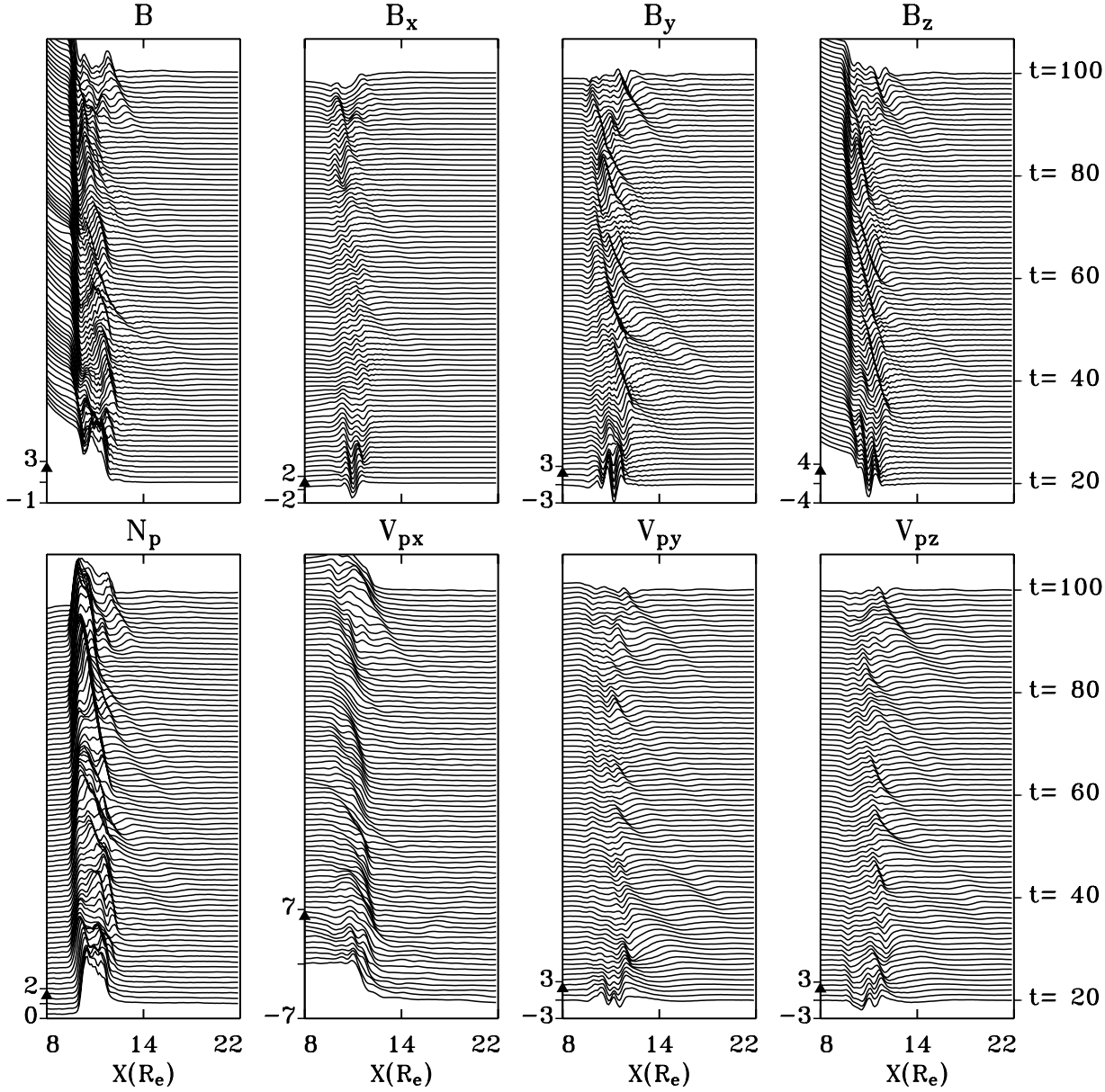

Figure 4. Spatial profiles of various quantities along the Sun-Earth line, in a time sequence from $t = 20$ to $t = 100$.

contours of the parallel ion temperature $T_{p\|}$, x-component of ion flow velocity V_{px}, magnetic field components B_y and B_z, and flow components V_{py} and V_{pz}. Upstream of the quasi-parallel shocks, the parallel temperature is enhanced due to the backstreaming ions at the shocks. Field-aligned temperature structures are also seen extending through the foreshock and downstream regions, with the increased (decreased) temperature corresponding to a decreased (increased) density and magnetic field. The flow velocity, which is mainly in the $-\mathbf{x}$ direction in the upstream, slightly decreases in the regions with the enhanced thermal energy, as seen in the upper right plot of Figure 3. The upstream structures in B_y and B_z, however, are quite different from those in B or N_p. They represent the electromagnetic waves that appear to be consistent with the beam whistler modes [e.g., *Winske et al.*, 1990]. These waves propagate with a wave vector nearly along the magnetic field, i.e., $\mathbf{k} \simeq \mathbf{k}_{\|} \simeq \mathbf{k}_{\mathbf{x}}$. Close to the shock front, the wave vectors become more oblique to the magnetic field direction at larger $|y|$ away from the Sun-Earth line and are nearly along the shock normal. Such feature indicates that the waves near the shock may be associated with the shock internal process or the shock reformation, a source that is different from the field-aligned beams. There is also a good correlation between V_{py} and B_y and between V_{pz} and B_z. In the quasi-parallel shock, near the subsolar area, the Rankine-Hugoniot jump conditions based on the magnetohydrodynamics (MHD) are found to be poorly satisfied. The shock appears to be turbulent due to the local wave packets, and it lacks a smooth shock front and a well-defined shock normal. On the other hand, the fits to shock jump conditions, including the temperature anisotropy [*Chao*, 1970], are much better at

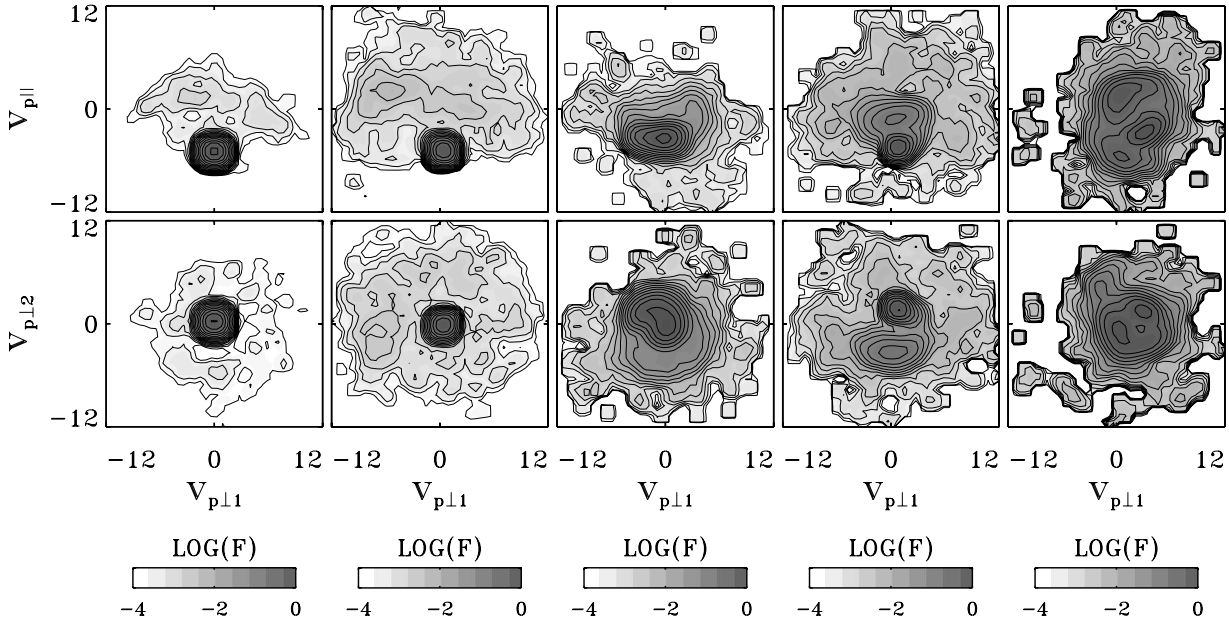

Figure 5. Left two columns: typical ion velocity distributions near the rim (left column) and core (second column) of a foreshock diamagnetic cavity. Third to last columns: typical ion distributions in the transition of quasi-parallel shock. The top row shows the distribution function F in the $v_{p||} - v_{p\perp 1}$ plane, where $v_{p||}$ is the parallel velocity of particles, and $v_{p\perp 1}$ is a perpendicular velocity component. The bottom row shows the distribution functions in the plane perpendicular to the magnetic field.

the quasi-perpendicular shock in $|y| > 15$, where the shock front is much smoother and no ion foreshock exists. The good fit is seen more clearly away from the equator because part of the front of the quasi-perpendicular shock is cut out in the equatorial plane. Note that across the bow shock, the jump in V_{px} becomes less significant at larger $|y|$ because of the more oblique inflow there relative to the shock normal.

[25] To examine the propagation speeds of foreshock waves and the shock reformation in our simulation, Figure 4 presents the spatial profiles of B, B_x, B_y, B_z, N_p, V_{px}, V_{py}, and V_{pz} along the Sun-Earth line, in a time sequence from $t = 20$ to $t = 100$. The low-frequency perturbations in B_y and B_z in the upstream beam whistler waves are seen to have an antiphase relation with V_{py} and V_{pz}, respectively, and are right-hand circularly or elliptically polarized in the solar wind plasma frame of reference. These waves are generated in the broad region of the foreshock. Note that small-amplitude perturbations in B and N_p may also appear in these waves. Some whistler waves are also generated near the shock transition. The upstream waves propagate sunward, with a wave speed $\sim 2V_{A0}$ in the solar wind frame of reference, smaller than the solar wind convection speed. Thus they are carried earthward by the solar wind.

[26] Meanwhile, the diamagnetic cavity structures in B and N_p are present. They are seen more clearly within $r < 15\ R_E$ in Figure 4, with amplitude $\Delta N/N \sim \Delta B/B \sim 20\%$ and parallel wavelength $\sim 3\ R_E$. They also propagate sunward with a speed of $\sim 2V_{A0}$ in the solar wind frame and thus a speed of $3\ V_{A0}$ in the simulation (Earth) frame of reference. Their speed is slowed down as they approach the shock front. The wavy structures in B are well correlated with those in B_x, indicating that the diamagnetic cavities are associated with compressional perturbations in magnetic field. Note that the correspondingly perturbations in the velocity V_{px} may alter the earthward moving speeds of the foreshock waves.

[27] The foreshock waves steepen into large-amplitude, more dynamic turbulence as they crash into the shock transition. The reformation (i.e., steepening) process of the bow shock thus follows the constant arrival of the foreshock waves. During the reformation cycle of the shock, the shock position oscillates within a width of $\sim 1-2\ R_E$. The period of the reformation cycle is $\sim 20\ \Omega_0^{-1}$. The downstream waves, while being slowed down, appear to be largely associated with the foreshock waves. Moreover, the magnetopause position also slightly oscillates in response to the foreshock pressure pulses.

[28] The ion velocity distributions associated with the foreshock cavities resemble those obtained from satellite observations [*Sibeck et al.*, 2002]. The left two columns of Figure 5 show the typical ion velocity distributions near the rim (left column) and core (second column) of a diamagnetic cavity in the foreshock region. The top row shows the phase space distribution function (F) in the $v_{p||} - v_{p\perp 1}$ plane, where $v_{p||} = \mathbf{v}_p \cdot \mathbf{b}$ is the particle velocity component parallel to the local magnetic field, $\mathbf{b}$ is the unit vector along the magnetic field, and $v_{p\perp 1} = \mathbf{v} \cdot (\mathbf{b} \times \mathbf{e}_y)/|\mathbf{b} \times \mathbf{e}_y|$ is a velocity component perpendicular to the magnetic field. The bottom row shows the distribution function in the $v_{p\perp 1} - v_{p\perp 2}$ plane perpendicular to the magnetic field, where $\mathbf{v}_{p\perp 2}$ is perpendicular to the plane containing $\mathbf{b}$ and $\mathbf{v}_{p\perp 1}$. The distribution function at each location is normalized by the peak of the phase space density at the location. In the rim region around the cavity, the ion distribution shows an incident solar wind plasma population centered at $v_{p||} = -5V_{A0}$ and a low-density hot beam of backstreaming ions, scattered and partially diffused. In the core of the cavity, the

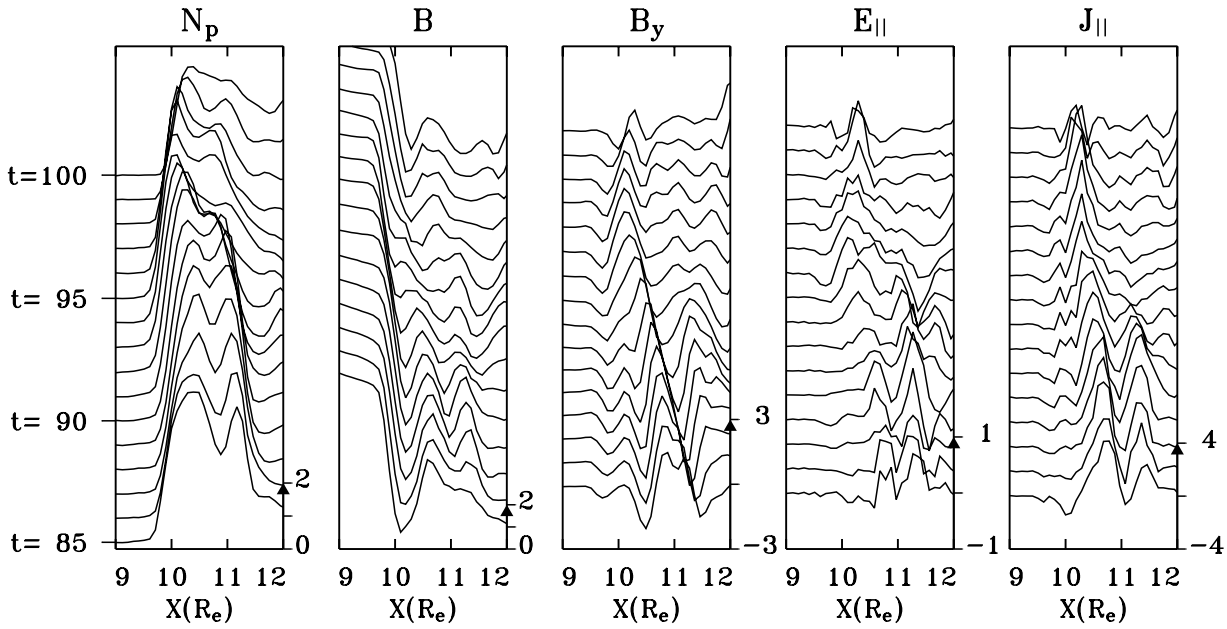

Figure 6. Highlight of spatial profiles of various quantities in the magnetosheath-magnetopause region, from $r = 9-12\ R_E$, along the Sun-Earth line during the time interval of $t = 85-100$.

hot ion beams are further accelerated and heated in both the parallel and perpendicular directions. The distribution is nearly isotropic in the perpendicular plane, whereas it is roughly a semicircular nonisotropic distribution in the parallel direction. Furthermore, the two populations of the solar wind plasma and the hot beam are still distinguished. These results are similar to those obtained from our previous 2-D simulation [*Lin*, 2003].

[29] The third to fifth columns of Figure 5 show the typical ion distributions obtained in the shock transition. The distribution shown in the third column, taken at $(r, \theta, \phi) = (13.0\ R_E,\ 65°,\ 75°)$, contains the incident solar wind population, which is somewhat heated, and the thermalized and accelerated downstream plasma population. On the other hand, the incident ions may also be reflected at the quasi-parallel shocks [e.g., *Gosling and Robson*, 1985]. The turbulent shock structure due to the interaction among the ion beams/plasma populations is found to lead to multiple ion beams. The fourth column, taken at $(r, \theta, \phi) = (13.0\ R_E,\ 75°,\ 75°)$ shows that a gyrating (in the perpendicular plane), reflected ion beam coexists with the incident solar wind and the hot downstream plasma. At the position shown in the right column, for $(r, \theta, \phi) = (13.0\ R_E, 60°, 75°)$, three ion populations/beams are present.

3.2. Generation of Kinetic Alfvén Waves Near the Magnetopause

[30] In the following, we discuss the generation of Alfvén waves near the magnetopause and in the magnetosphere due to the foreshock waves. As the pressure pulses approach the magnetopause, part of the compressional waves are transmitted into the magnetosphere. In addition, the compressional waves are coupled to the transverse Alfvén modes near the magnetopause boundary and in the magnetosphere, where the magnetic field and/or density are highly nonuniform [*Chen and Hasegawa*, 1974; *Southwood*, 1974]. First, shear Alfvén waves are generated at the magnetopause and in the magnetosphere due to the Alfvén resonance condition, $\omega = \omega_A \equiv k_{||} V_A$, where ω is the frequency of a compressional wave mode in the incident wave packet and $k_{||}$ is the parallel wave number of the Alfvén wave. The resonant coupling coefficient between the compressional wave and the transverse Alfvén wave is determined by the spatial gradients in V_A and $k_{||}$. As predicted by the above theories and reported by many observations [e.g., *Walker and Greenwald*, 1980; *Takahashi and McPherron*, 1982], the process leads to the resonance of closed field lines in the dipole field, as to be shown in the next subsection. Second, mode conversion to short-wavelength kinetic Alfvén waves [*Hasegawa and Chen*, 1976; *Lee et al.*, 1994; *Johnson and Cheng*, 1997], or Alfvén waves with finite ion gyroradius correction, is seen near the magnetopause boundary, where $k_\perp \gg k_{||}$ and the transverse wave energy is built up at $k_\perp \rho_i \sim 1$, where ρ_i is the ion Larmor radius. The generation of KAWs takes place after that of shear Alfvén waves.

[31] Figure 6 shows the highlight of various quantities in the magnetosheath-magnetopause region, from $r = 9$ to $12\ R_E$, along the Sun-Earth line during the time interval $t = 85-100$. At $t = 85$, the bow shock is centered around $r = 11.5\ R_E$. A diamagnetic cavity, with a low density and low magnetic field in its center, propagates in the magnetosheath, as seen from the profiles of N_p and B. At $t = 91$, this perturbation has reached the magnetopause and is interacting with the magnetopause boundary region as a pressure pulse. The magnetopause boundary is centered around $r \sim 10\ R_E$, with a width of $\sim 1\ R_E$ and a strong gradient in the density and magnetic field. The wave transmission into the magnetosphere and the generation of shear Alfvén waves, which is seen more clearly along the field lines of the dipole field, will be discussed in the next subsection. On the other hand, perturbations in B_y (and the associated $J_{||}$) in the

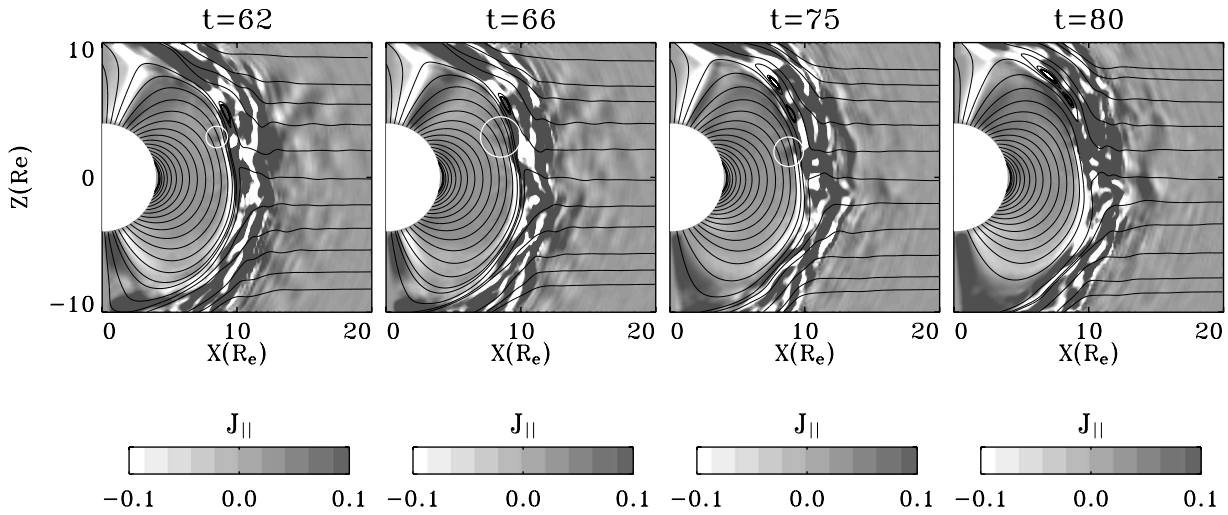

Figure 7. Parallel current density ($J_{||}$) contours and field line traces in a portion of the noon-midnight meridian plane at four different times. Some of the local enhancements of $J_{||}$ in the magnetosphere are highlighted by white circles.

magnetosheath waves are also propagating toward the magnetopause.

[32] At $t \geq 97$, a KAW pulse appears to have formed around $r = 10.2\ R_E$ in the boundary layer due to the pressure pulse. At this location, the **B** field points mainly in the z direction, perpendicular to the radial coordinate line. The amplitudes of the transverse B_y and B_x (not shown) and $J_{||}$ increase locally in the wave pulse. The B field has a sharp dip in the trapped KAW, while the density is enhanced. Thus the in-phase relation between B and N in the foreshock cavities has now evolved to an antiphase relation. A strong enhancement is also seen in the amplitude of the parallel electric field $E_{||} = -\nabla_{||} p_e/N = -T_e \nabla_{||} N/N$, as well as E_x. This $E_{||}$ is generated locally and not related to the $E_{||}$ structures near the shock transition. The KAW pulse has a short wavelength compared with the magnetosheath waves, as seen in Figure 6, with **k** dominantly $\perp$ **B**. For $\rho_i \simeq 0.1\ R_E$ and $\lambda \simeq 0.6$–$1\ R_E$ found in this region, $k_\perp \rho_i \simeq 0.6$–$1.0$.

[33] In the theories of mode conversion to KAW [e.g., *Johnson and Cheng*, 1997], the KAW propagates backward against the incident pressure pulses, into the high-density magnetosheath. The wave power can then either be trapped at the location of $k_{||} = 0$, under a southward IMF, or be absorbed by the ion or electron Landau damping. In our 3-D global simulation, the KAW does not propagate sunward into the magnetosheath because of the earthward flow convection in the magnetosheath. As a result, the wave is trapped near the magnetopause and meanwhile is also subject to ion Landau damping in this region with ion $\beta_p \sim 2$–6. The ions are heated in both parallel and perpendicular directions. The electron Landau damping, however, does not exist in this hybrid simulation code.

[34] The KAW shown in Figure 6 disappears from the subsolar area at $t > 100$ as it is carried away by the tailward convection. Such process of the generation of kinetic Alfvén waves reoccurs with the frequent arrivals of pressure pulses at the magnetopause and is seen at at various latitudes and longitudes. The finite $E_{||}$ generated in the KAWs is believed to be important in the acceleration of electrons in the magnetosphere, which is beyond the scope of the present model.

3.3. Generation of Shear Alfvén Waves and Field Line Resonance in the Magnetosphere

[35] As mentioned above, the generation of shear Alfvén waves, and the associated field-aligned currents, follows the arrival of the compressional waves. Figure 7 shows the contours of $J_{||}$ in a portion of the noon-midnight meridian plane at four different times. The field lines traces are also superposed on the contours. Note that the field line traces are only for the field components (B_x and B_z) in this 2-D meridian plane and thus may not present the precise field topology. The parallel currents seen in local areas upstream and downstream of the bow shock are associated with the field perturbations in the transverse electromagnetic waves around the bow shock. These waves are also convected to the magnetopause vicinity, but they do not propagate across the field lines into the magnetosphere. In the magnetopause boundary layer, parallel currents are produced by the boundary flow vorticity (consistent with the senses of region-1 currents but not clear in the noon-midnight meridian plane), magnetic reconnection, or the foreshock pressure pulses. For example, excitation of a negative $J_{||}$ is seen near the high-latitude reconnected flux tubes on the dayside, and this structure propagates northward with the flux tubes. This parallel current later leaks into the cusp as the field line topology changes during the tailward covection across the cusp.

[36] The production of magnetospheric $J_{||}$ following the impinging of the pressure pulses on the magnetopause can be seen in Figure 7. In the outer part of the magnetopause boundary layer, where the compressional waves first make the impact, strong Alfvén waves and parallel currents frequently appear and propagate along the magnetopause. Some leak into the cusp magnetosphere in both hemispheres. The patterns and polarities of $J_{||}$ in the magnetopause and the cusps are seen to change with time. On the other hand, as the fast mode compressional waves propagate

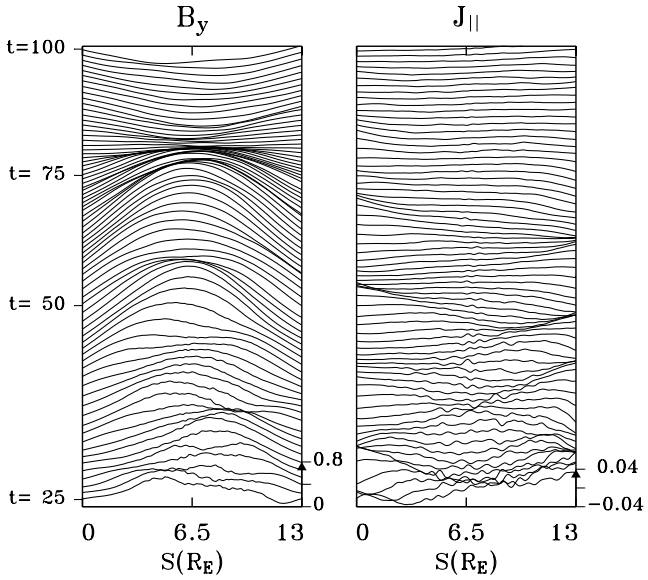

Figure 8. Time sequence of the longitudinal magnetic field component (left column) and the parallel current density (right) along the field lines at $L = 7.5$ in the noon-midnight meridian plane as a function of S, where S is the distance along the field line from south to north. In this meridian plane, $B_y = -B_\phi$.

across the field lines and penetrate into the geomagnetic dipole field, they excite local shear Alfvén waves and thus $J_{||}$ in the inner magnetosphere. At $t = 62$, as seen in the first column of Figure 7, a positive enhancement of $J_{||}$ appears around $(x, z) = (8.5\ R_E, 3.0\ R_E)$, inside the white circle. The production of this $J_{||}$ follows the arrival of a pressure pulse, which causes a local compression of the magnetopause, as seen from the shape of the field lines. At $t = 66$, the area of this local $J_{||}$ has further extended into the dipole field, again shown in the while circle, as the waves penetrate deeper. Meanwhile, the $J_{||}$ current has propagated along the field lines and thus spread out. Such local production of $J_{||}$ is very frequent. As shown in the third column of Figure 7, another $J_{||}$ current is generated at $t = 75$ around $(x, z) = (8.8\ R_E, 1.9\ R_E)$, as marked by the white circle, following a new pressure pulse. By $t = 80$, this parallel current and those generated nearby have occupied a wide region along the field lines. Meanwhile, shear Alfvén waves and field-aligned currents have also been generated in the southern hemisphere, while again originated near the equatorial area. The transient currents $J_{||}$ due to the pressure pulses are found to propagate in both directions along the field lines, and both positive and negative polarities are seen in either hemisphere during the simulation.

[37] The propagation of shear Alfvén waves in the inner magnetosphere leads to the field line resonance, which is seen at radial distances away from the magnetopause boundary. Figure 8 shows time sequence of the azimuthal (longitudinal) magnetic field component and the parallel current density $J_{||}$ along the field lines through the equatorial radius of $L = 7.5$ in the noon-midnight meridian plane ($\phi = 90°$) as a function of S, where S is the distance along the field line, with the starting point $S = 0$ (13 R_E) approximately at the $r = 4\ R_E$ boundary in the south (north). Note that $B_y = -B_\phi$ in this meridian plane. The tick marks on the right-side vertical axis of each plot only represent the scale of the corresponding quantity at $t = 25$, but the amplitude of perturbation in all times of the sequence is scaled proportionally. Note that the selected field line (flux tube) is only approximately the same line at different times, as the magnetospheric field undergoes a low-frequency oscillation in response to the foreshock oscillations. In response to the compressional waves, which constantly arrive in the equatorial region, the perturbation in the transverse B_y, as well as in $J_{||}$ corresponding to the transverse distortion of field lines, is present and bounces between the south and north boundaries in $t < 50$. The perturbation corresponds to multiple modes in $k_{||}$ between the polar boundaries. At $t > 50$, the nearly standing wave pattern is reached, while the wavelength corresponds to a 1/2 wave number between the boundary ends, i.e., the fundamental odd resonance mode. Correspondingly, the resonance frequency is found to satisfy $\omega \simeq \omega_A = V_A k_{||}$, consistent with the resonance period of $T \simeq 50$ in the simulation. At $t = 100$, the B_y oscillation starts another cycle of the resonance.

[38] Similar evolutions/patterns of the transverse field are also seen at all the other meridians, but the times to reach the stationary wave pattern are different. The resonance frequency increases with the decreasing distance L (increasing $k_{||}$), as frequently reported by satellite observations. The oscillation of the magnetic field in the field line resonance is seen predominantly in the azimuthal (toroidal) direction. No global cavity modes are found in our simulation. Only field line resonance modes in B_ϕ appear in response to the incoming compressional waves, while no wave harmonics are present in B_r.

[39] Different from previous MHD simulations [*Lee and Lysak*, 1991], this field line resonance is driven by the compressional wave pulses that are self-consistently and constantly generated at the foreshock of the quasi-parallel shocks. The driving sources are distributed globally, with multiple wave pulses arriving at various times and spatial locations, while each pulse has a local azimuthal extent. The final selection of the smallest resonance wave number, with $k_{||}\Delta S \simeq \pi$ and ΔS being the total length of the field line, in our simulated field line resonance may be due to that the source perturbations from the foreshock are mainly located near the equator, while the source frequency is low but broadband. The patterns of field line resonance driven by the foreshock pressure pulses under other IMF cone angles and Mach numbers will be investigated in our future study.

4. Summary

[40] In summary, we have carried out a self-consistent 3-D global hybrid simulation for a case with IMF along B_x. The investigation has been conducted for the quasi-parallel bow shock and its coupling to the dayside magnetosphere through foreshock waves. The main results are given below.

[41] 1. Electromagnetic whistler waves and diamagnetic cavities are generated in the foreshock of the quasi-parallel shock, where the reflected and leakage/backstreaming ion beams interact with the incoming solar wind. The structure of the upstream whistler waves is consistent with previous hybrid simulation. The magnetic field and density have an in-phase correlation in the foreshock cavities and their

surroundings, with decreased (increased) B and N_p at the center (rim) of cavity. The ion temperature increases in the cavities. The ion velocity distributions associated with the foreshock cavities show the existence of hot, partially diffused ion beam and the colder solar wind plasma, which resembles those obtained in satellite observations. Similar to our previous 2-D simulations, these cavity structures later develop into field-aligned density and magnetic field structures, with alternate field-aligned cavities (decrease in N_p) and filaments (increase in N_p). However, their structure, with perpendicular wavelength $\lambda \sim 20-80\ c/\omega_{pi}$, is three-dimensional.

[42] 2. The shock is constantly going through a reformation process, with reformation period $\sim 20\ \Omega_0^{-1}$. The magnetopause position also oscillates slightly due to the shock reformation.

[43] 3. As the foreshock compressional waves propagate to the dayside magnetopause, they interact with the magnetosphere as pressure pulses. The pulses associated with the foreshock cavities cause strong surface perturbations at the magnetopause. The compressional waves are found to mode convert to shear Alfvén waves in the magnetosphere, as predicted by theories. Field-aligned currents are produced correspondingly. Field line resonances are generated in the dipole field due to the shear Alfvén waves. In the case shown, the field line resonance is saturated at the fundamental wave number $k_\parallel \Delta S \simeq \pi$ and the resonance period $\omega \simeq \omega_A = V_A k_\parallel$. On the other hand, no global cavity mode is found in the simulation.

[44] 4. In addition, the incident compressional waves are found to mode convert to short-wavelength kinetic Alfvén waves at the magnetopause boundary, where the wave energy is built up at $k_\perp \rho_i \sim 1$. These KAWs are localized and trapped in front of the magnetopause. The parallel electric field is excited locally in the KAW.

[45] It should be noted that while this first 3-D global hybrid simulation study reveals the interaction between the bow shock and the magnetosphere, the simulation model used in this study is limited only to the dayside plasma region. The magnetotail and its response, which should become more important to the global dynamics at time $t \gg$ the dayside Alfvén convection time, are not included. In addition, the realistic density profile in the plasmasphere is not considered. This may affect the detailed features of the magnetospheric field line resonance.

[46] Finally, owing to the numerical stability consideration, the density used in the inner magnetosphere results in that the rise of V_A with the decreasing r is slower than the rise in reality. Thus the ratio of the magnetospheric to magnetopause Alfvén speeds is smaller than reality. This problem of the seemingly small V_A in the magnetosphere is compensated by the usage of a solar wind Alfvén speed larger than reality. As a consequence, V_A in the magnetosphere (e.g., $r = 7.5\ R_E$) in this study is approximately equal to the realistic value. With the incident compressional mode frequency ω scaled to the realistic Ω_0 used in the simulation, and considering the nearly realistic V_A and global $k_\parallel$ in the simulated magnetosphere, the resulting mode conversion to shear Alfvén waves is expected to reflect the global physics based on the right scales. We have also run a similar case but with a larger density and thus V_A is reduced by 1/2 in the magnetosphere, while maintaining the same V_{A0} in the solar wind. The results of field line resonance are similar to those shown in this paper, with the same resonance wave number, only the resonance frequency is reduced by 1/2. It would be interesting to examine the patterns of the field line resonance under an oblique IMF and with more realistic parameters.

[47] **Acknowledgments.** This work was supported by NASA grant NAG5-12899 and NSF grant ATM-0213931 to Auburn University. Computer resources were provided by the Arctic Region Supercomputer Center. The authors thank D. W. Swift for helps in the development of the 3-D hybrid code.

[48] Lou-Chuang Lee thanks Dan Winske for the assistance in evaluating this paper.

References

Chao, J. K. (1970), Interplanetary collisionless shock waves, *Rep. CSR TR-70-3*, Cent. for Space Res., Mass. Inst. of Technol., Cambridge, Mass.

Chen, L., and A. Hasegawa (1974), A theory of long-period magnetic pulsations: 1. Steady state excitation of field line resonance, *J. Geophys. Res.*, *79*, 1024.

Dubouloz, N., and M. Scholer (1995), Two-dimensional simulations of magnetic pulsations upstream of the Earth's bow shock, *J. Geophys. Res.*, *100*, 9461.

Engebretson, M. J., N. G. Lin, W. Baumjohann, H. Luehr, B. J. Anderson, L. J. Zanetii, T. A. Potemra, R. L. McPherron, and M. G. Kivelson (1991), A comparison of ULF fluctuations in the solar wind, magnetosheath, and dayside magnetosphere: 1. Magnetosheath morphology, *J. Geophys. Res.*, *96*, 3441.

Fairfield, D. H., W. Baumjohann, G. Paschmann, H. Luhr, and D. G. Sibeck (1990), Upstream pressure variations associated with the bow shock and their effects on the magnetosphere, *J. Geophys. Res.*, *95*, 3773.

Fuselier, S. A., M. F. Thomsen, F. M. Ipavich, and W. K. H. Schmidt (1995), Superthermal He^{2+} in the Earth's foreshock region, *J. Geophys. Res.*, *100*, 17,107.

Gosling, J. T., and A. E. Robson (1985), Ion reflection, gyration, and dissipation at supercritical shocks, in *Collisionless Shocks in the Heliosphere: Reviews of Current Research*, *Geophys. Monogr. Ser.*, vol. 35, edited by B. T. Tsurutani and R. G. Stone, p. 141, AGU, Washington, D. C.

Hasegawa, A., and L. Chen (1976), Kinetic processes in plasma heating by resonance mode conversion of Alfvén wave, *Phys. Fluids*, *19*, 1924.

Hoppe, M. M., C. T. Russell, L. A. Frank, T. E. Eastman, and E. W. Greenstadt (1981), Upstream hydromagnetic waves and their association with backstreaming ion populations: ISEE 1 and 2 observations, *J. Geophys. Res.*, *86*, 4471.

Johnson, J. R., and C. Z. Cheng (1997), Kinetic Alfvév waves and plasma transport at the magnetopause, *Geophys. Res. Lett.*, *24*, 1423.

Krauss-Varban, D. (1995), Waves associated with quasi-parallel shocks: generation, mode conversion, and implications, *Adv. Space Res.*, *15*(8/9), 271.

Lee, D.-H., and R. L. Lysak (1991), Impulsive excitation of ULF waves in the three-dimensional dipole model: The initial results, *J. Geophys. Res.*, *96*, 3479.

Lee, L. C., J. R. Johnson, and Z. W. Ma (1994), Kinetic Alfvén waves as a source of plasma transport at the dayside magnetopause, *J. Geophys. Res.*, *99*, 17,405.

Lin, Y. (2003), Global-scale simulation of foreshock structures at the quasi-parallel bow shock, *J. Geophys. Res.*, *108*(A11), 1390, doi:10.1029/2003JA009991.

Russell, C. T., J. G. Luhmann, T. J. Odera, and W. F. Stuart (1983), The rate of occurrence of dayside Pc 3, 4 pulsations: The L-value dependence of the IMF cone angle effect, *Geophys. Res. Lett.*, *10*, 663.

Scholer, M. (1993), Upstream waves, schocklets, short large-amplitude magnetic structures and the cyclic behavior of oblique quasi-parallel collisionless shocks, *J. Geophys. Res.*, *98*, 47.

Scholer, M., and T. Terasawa (1990), Ion reflection and dissipation at quasi-parallel collisionless shocks, *Geophys. Res. Lett.*, *17*, 119.

Schwartz, S. J., and D. Burgess (1991), Quasi-parallel shocks: A patchwork of three-dimensional structures, *Geophys. Res. Lett.*, *18*, 373.

Schwartz, S. J., D. Burgess, W. P. Wilkinson, R. L. Kessel, M. Dunlop, and H. Luhr (1992), Observations of short large-amplitude magnetic structures at a quasi-parallel shock, *J. Geophys. Res.*, *97*, 4209.

Sckopke, N., G. Paschmann, S. J. Bame, J. Gosling, and C. T. Russell (1983), Evolution of ion distributions across the nearly perpendicular

bow shock: Specularly and nonspecularly reflected ions, *J. Geophys. Res.*, *88*, 6121.

Sibeck, D. G., et al. (1989), The magnetospheric response to 8-minute-period strong-amplitude upstream pressure variations, *J. Geophys. Res.*, *94*, 2505.

Sibeck, D. G., R. B. Decker, D. G. Mitchell, A. J. Lazarus, R. P. Lepping, K. W. Ogilvie, and A. Szaba (2001), Solar wind preconditioning in the flank foreshock: IMP-8 observations, *J. Geophys. Res.*, *106*, 21,675.

Sibeck, D. G., T.-D. Phan, R. Lin, R. P. Lepping, and A. Szabo (2002), Wind observations of foreshock cavities: A case study, *J. Geophys. Res.*, *107*(A10), 1271, doi:10.1029/2001JA007539.

Sibeck, D. G., N. B. Trivedi, E. Zesta, R. B. Decker, H. J. Singer, A. Szabo, H. Tachihara, and J. Watermann (2003), Pressure-pulse interaction with the magnetosphere and ionosphere, *J. Geophys. Res.*, *108*(A2), 1095, doi:10.1029/2002JA009675.

Southwood, D. J. (1974), Some features of field line resonances in the magnetosphere, *Planet. Space Sci.*, *22*(3), 483–491.

Swift, D. W. (1996), Use of a hybrid code for a global-scale plasma simulation, *J. Comput. Phys.*, *126*, 109.

Takahashi, X., and X. McPherron (1982), Harmonic structure of Pc 3-4 pulsations, *J. Geophys. Res.*, *87*, 1504.

Tanaka, M., C. C. Goodrich, D. Winske, and K. Papadopoulos (1983), A source of backstreaming ion beams in the foreshock region, *J. Geophys. Res.*, *88*, 3046.

Thomas, V. A., and S. H. Brecht (1988), Evolution of diamagnetic cavities in the solar wind, *J. Geophys. Res.*, *93*, 11,341.

Thomas, V. A., D. Winske, and N. Omidi (1990), Reforming supercritical quasi-parallel shocks: 1. One and two dimensional simulations, *J. Geophys. Res.*, *95*, 18,809.

Walker, A. D. M., and R. A. Greenwald (1980), Pulsation structure in the ionosphere derived from auroral radar data, *J. Geomagn. Geoelectr.*, suppl. 2, *32*, 111.

Wibberenz, G., F. Zollich, H. M. Fischer, and K. Keppler (1985), Dynamics of intense upstream ion events, *J. Geophys. Res.*, *90*, 283.

Winske, D., N. Omidi, K. B. Quest, and V. A. Thomas (1990), Reforming supercritical quasi-parallel shocks: 2. Mechanism for wave generation and front reformation, *J. Geophys. Res.*, *95*, 18,821.

Y. Lin and X. Y. Wang, Physics Department, Auburn University, 206 Allison Laboratory, Auburn, AL 36849-5311, USA. (ylin@physics.auburn.edu; xywang@physics.auburn.edu)